Chiral π-Conjugated Double Helical Aminyl Diradical with Triplet Ground State

Haoxin Guo[†], Joshua B. Lovell[§], Chan Shu[†,‡], Maren Pink[#], Martha Morton[†], Suchada Rajca[†], and Andrzej Rajca*[†]

[†]Department of Chemistry, University of Nebraska, Lincoln, Nebraska 68588-0304, United States.

[§] Teledyne ISCO, 4700 Superior St, Lincoln, Nebraska 68504-1328, United States.

[#]IUMSC, Department of Chemistry, Indiana University, Bloomington, Indiana 47405-7102, United States.

[‡] Current address: Toyota Research Institute of North America, 1555 Woodridge Avenue, Ann Arbor, Michigan 48105, United States.

ABSTRACT: We report a neutral high-spin diradical of chiral C_2-symmetric bis[5]diazahelicene with $\Delta E_{ST} \approx 0.4$ kcal mol^{-1}, as determined by EPR spectroscopy/SQUID magnetometry. The diradical is the most persistent among all high-spin aminyl radicals reported to date by a factor of 20, with a half-life up to 6 days in 2-MeTHF at room temperature. Its triplet ground state and excellent persistence may be associated with the unique spin density distribution within the dihydrophenazine moiety, characterizing two effective 3-electron C-N bonds analogous to the N-O bond of nitroxide radical. The enantiomerically enriched (ee ≥ 94%) (*MM*)- and (*PP*)-enantiomers of the precursors to the diradicals are obtained by either preparative chiral supercritical fluid chromatography (SFC) or resolution via functionalization with chiral auxiliary of the C_2-symmetric racemic tetraamine. The barrier for racemization of the solid tetraamine is $\Delta G^{\ddagger} = 43 \pm 0.01$ kcal mol^{-1} in the 483 – 523 K range. The experimentally estimated lower limit of the barrier for racemization of diradical, $\Delta G^{\ddagger} \geq 26$ kcal mol^{-1} in 2-MeTHF at 293 K, is comparable to the DFT-determined barrier of $\Delta G^{\ddagger} = 31$ kcal mol^{-1} in the gas phase at 298 K. While the enantiomerically pure tetraamine displays strong chiroptical properties, with anisotropy factor $|g| = |\Delta\varepsilon|/\varepsilon = 0.036$ at 376 nm, $|g| \approx 0.005$ at 548 nm of the high-spin diradical is comparable to that recently reported triplet ground state diradical dication. Notably, the radical anion intermediate in the generation of diradical exhibits large SOMO-HOMO inversion, SHI = 35 kcal mol^{-1}.

INTRODUCTION

Chiral π-conjugated molecules with open-shell structure have great potential in the development of material to enable technological innovations.[1-3] The concurrent intrinsic helical chirality and electron spin coupling is a compelling molecular property for the development of novel organic optoelectronic materials and devices. Nevertheless, only a handful open-shell helical radicals and radical ions have been prepared and studied to date, and all of them were possessing either S = ½ or low-spin S = 0 ground state.[4-19] Among the elegant examples are S = ½ neutral aminyl radicals of [4]helicene and [7]helicene, in which the nitrogen- and carbon-centered radicals with spin density delocalized within helical π-systems (Figure 1).[4,5]

It is conceivable that the coexistence of strong molecular chirality and high-spin ground state could benefit the development of novel spin filters.[1,20] Notably, the diamagnetic [5]-, [6]-, and [7]helicene derivatives with spin polarizations of ≤80% were studied.[21-23] High-spin diradicals were theoretically predicted to provide up to 100% spin polarizations,[24,25] and recently, large magnetoresistance in an open-shell diradical polymer was discovered.[26]

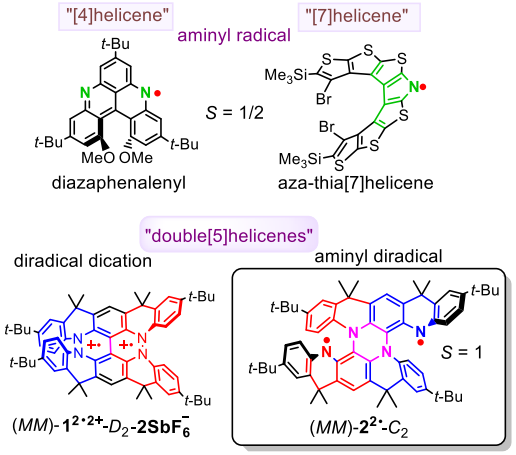

Figure 1. S = ½ helical aminyl radicals and double helical S = 1 diradicals.

Recently, we reported the first high-spin organic diradical within a double helical π-system, diradical dication (*MM*)-**1²•2+**-D_2-2SbF$_6^-$ (Figure 1).[27] However, the interference from the counterions could make it impractical to form a well-defined thin film.[28-31] The convergence of the triplet ground state with helical π-systems, anticipated to enhance spin filter efficiency, may be achieved

through neutral diradicals (and polyradicals) that are likely to possess a favorable ability to create high-quality thin films.

We were elated to serendipitously discover the high-spin aminyl diradical (*MM*)-**2²•**-C_2 (Figure 1). Based on Ovchinnikov's model of alternating atom connectivity,[32,33] diradical **2²•**-C_2 should have a singlet ground state, that is, the 1,5-connected phenazine or 1,5-connected 9,10-dihydrophenazine should act as an antiferromagnetic coupling unit (ACU) (Figure 2). However, our DFT computations show that **2²•**-C_2 has a triplet ground state with a singlet-triplet energy gap, ΔE_{ST} = 0.67 kcal mol^{-1}. We notice that the structure of **2²•**-C_2 consists of two effective 3-electron C-N bonds, analogous to the N-O bonds in nitroxide radicals.[1,34] Therefore, it can be rationalized that the 1,5-connected 9,10-dihydrophenazine is an effective ferromagnetic coupling unit (FCU) (Figure 2), and thus the presence of significant ferromagnetic coupling is observed. Importantly, this unique structural feature akin to nitroxide may provide excellent radical stability.

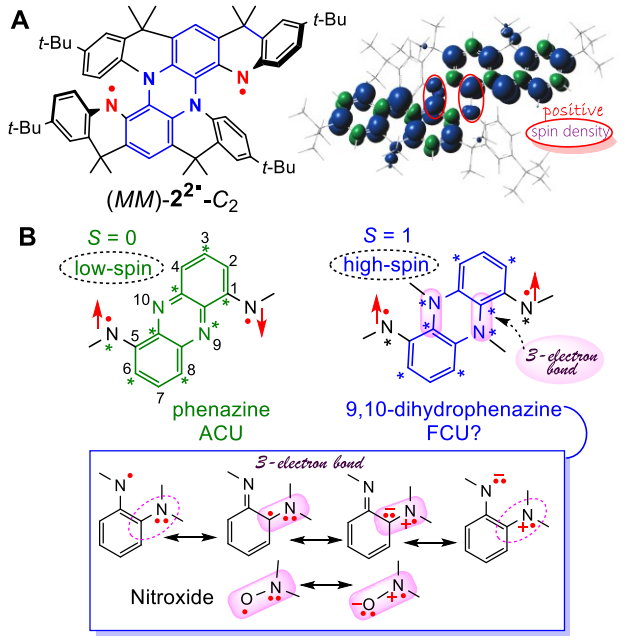

Figure 2. A: Diradical (*MM*)-**2²•**-C_2, with blue-highlighted 9,10-dihydrohydrazine core moiety, and its spin density map at the UB3LYP/6-31G(d,p) level of theory; positive (blue) and negative (green) spin densities are shown at the isodensity level of 0.002 electron Bohr^{-3}. **B**: 9,10-Dihydrophenazine as an FCU because of the positive spin densities within N9-C and N10-C fragments (highlighted with pink ovals), caused by the resonance within 3-electron bonds analogous to that in a nitroxide radical.

Herein we report the synthesis, magnetic and chiroptical characterization of high-spin (*S* = 1) aminyl diradical **2²•**-C_2 and its enantiomers (*MM*) and (*PP*) (Figure 1). In addition, we describe practical resolutions of the tetraamine **2**-H_2-C_2, direct precursor to the diradical, using either a chiral auxiliary or preparative chiral supercritical fluid chromatography (SFC). Notably, (*MM*)-**2²•**-C_2, with ΔE_{ST} = 0.42 ± 0.02 kcal mol^{-1}, is by far the most persistent among all high-spin aminyl diradicals with a half-life, $\tau_{1/2}$ = 5.77 ± 0.11 d in 2-methyltetrahydrofuran (2-MeTHF) under vacuum at room temperature.

RESULTS AND DISCUSSION

Synthesis. We discovered the tetraamine **2**-H_2-C_2 in the process of optimizing the oxidation reaction of diamine **3** to **1**-D_2 (Scheme 1). We noticed that when using <1 equiv of oxidant such as benzoyl peroxide, in addition to C-C and (N-N)$_2$ triply-coupled **1**-D_2 and C-C mono-coupled **1**-H_4 products,[35] a C_2-symmetric (C-N)$_2$ di-coupled **2**-H_2-C_2 product may be isolated in about 20% yield. Remarkably, these oxidations lead to near perfect diastereoselectivity for **1**-D_2[27,35] and **2**-H_2-C_2 vs. C_{2h}- and C_i-symmetric *meso*-isomers, respectively.

Scheme 1. Synthesis and resolution of *rac*-2-H_2-C_2.

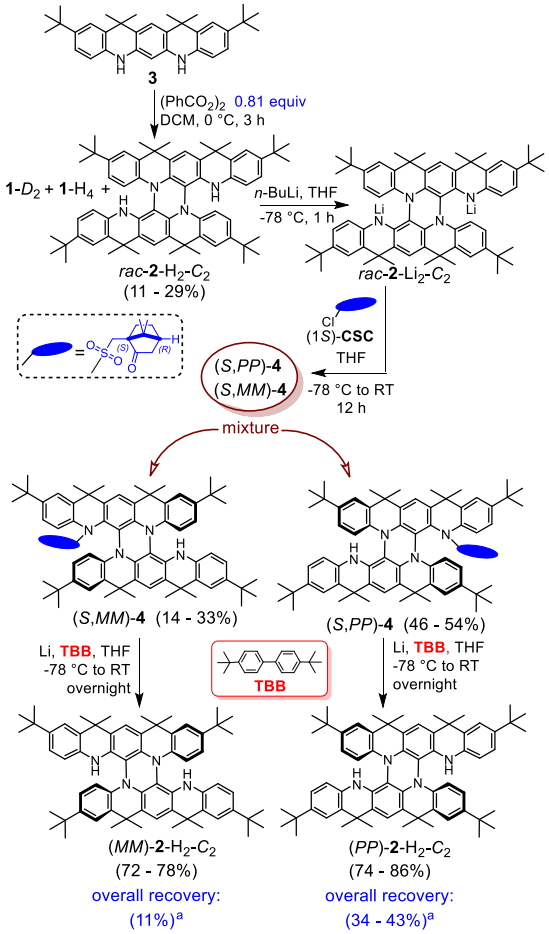

[a] Overall recovery for enantiomers with %ee of 94.0 – 97.4.

To resolve the racemic mixture of (*PP*)- and (*MM*)-**2**-H_2-C_2, the racemate is reacted with *n*-BuLi, to produce di-lithiated intermediate *rac*-**2**-Li_2-C_2, which is then quenched with (1*S*)-(+)-10-camphorsulfonyl chloride ((1*S*)-**CSC**); after workup, two mono-coupled diastereomers (*S*,*PP*)- and (*S*,*MM*)-**4** are isolated. (Among classic chiral auxiliaries used for resolution of [n]helicenes are chiral siloxanes and sulfoxides.[36-39]) Small amounts of sterically encumbered di-coupled diastereomers (*SS*,*PP*) and (*SS*,*MM*) are also observed by TLC and in ^{1}H NMR and mass spectra of crude reaction mixtures. After separation of (*S*,*PP*)- and (*S*,*MM*)-**4** using deactivated silica[40] column under ambient pressure, the reductive removal step of the chiral auxiliary (sulfonyl group) by dilithiated (dianion of) 4,4'-di-*tert*-butylbiphenyl[41-43] gives enantiomers (*MM*)- and (*PP*)-**2**-H_2-C_2 with isolated yields of ≤78 and ≤86%, respectively. The major enantiomer (*PP*) has an enantiomeric excess, ee ≥ 97%, based on the chiral SFC analysis (Figs. S1.39 and S1.41, SI).

The near baseline resolution of (*rac*)-**2**-H_2-C_2 in analytical chiral SFC prompted us to explore preparative chiral SFC. The primary

advantage of SFC over traditional HPLC originates in much larger binary diffusion coefficients in low viscosity CO_2, compared to classical LC phases, leading to a decrease in the separation time by a factor of about 5 while maintaining the same separation efficiency.[44,45] Starting from ca. 50 mg of racemate, in about 8 h, we could recover 57% and 82% of (*PP*)- and (*MM*)-enantiomers with ee ≥ 94%, respectively. In comparison, the chiral auxiliary approach, with an incomparably greater effort, provided lower recovery yields of ≤43% (*PP*) and ~11% (*MM*) (Scheme 1 and SI).

Aminyl diradicals *rac*-, (*PP*)- and (*MM*)-**2²•**-C_2 are generated from the corresponding tetraamines using our established two-step procedure:[46-49] (1) the reaction of tetraamine with *n*-BuLi (2+ equiv) in THF/hexane provides the corresponding dianion, and (2) following solvent exchange at low temperature to 2-MeTHF, the dianion is oxidized to the diradical by addition of I_2 via vacuum transfer, typically, with subsequent monitoring of reaction progress by EPR spectroscopy (Scheme 2).

Scheme 2. Aminyl diradicals: generation and decay in 2-MeTHF.

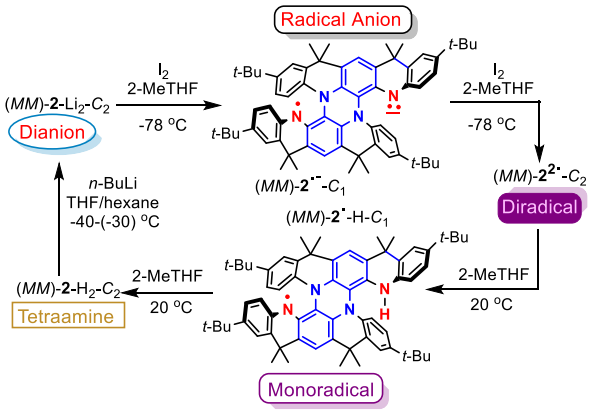

X-ray crystallography. X-ray structure of tetraamine *rac*-**2**-H_2-C_2 shows clearly that the molecule adopts an approximate C_2-symmetric conformation in the crystal (Figure 3). Two secondary amine moieties are nearly coplanar, as indicated by small rms deviation from the plane of 0.283 Å for the least-squares plane, defined by the N1-N4 and C8-C10, C18-C20, C40-C42, and C50-C52 atoms, i.e., the dihydrophenazine moiety and N2/N4. As it is likely that this coplanarity is maintained in the diradical **2²•**-C_2, it will be conducive to a strong exchange coupling between two aminyl radicals centered at N2 and N4.

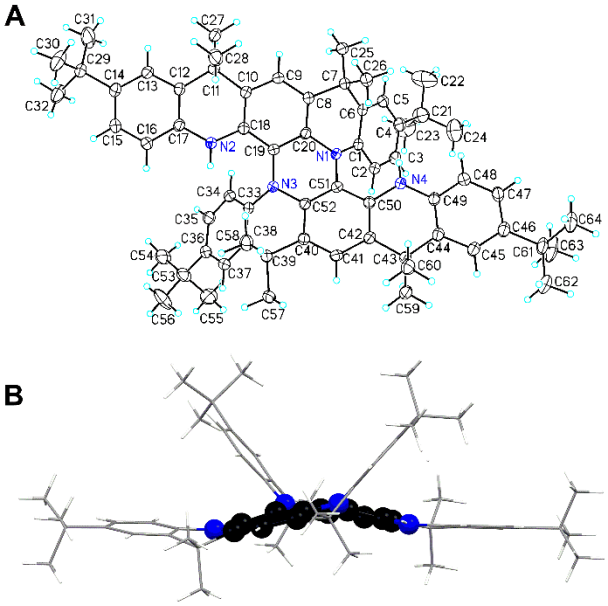

Figure 3. Single crystal X-ray structure of tetraamine *rac*-**2**-H_2-C_2; disorder of *tert*-butyl groups is omitted for clarity. **A**: Ortep plot with carbon and nitrogen atoms depicted using thermal ellipsoids set at the 50% probability level. **B**: Side view of the molecule with dihydrophenazine moiety, N2, and N4 shown in ball-and-stick. Additional data can be found in the SI: Table S1 and Figs. S1–S6.

EPR spectroscopy. EPR spectra of diradical *rac*-**2²•**-C_2 in 2-MeTHF/toluene, 1 : 3.41 in the 110 – 152 K range indicate a significant population of the triplet ground state. The product of paramagnetic susceptibility (χ) and temperature (T), $\chi T = 0.923 \pm 0.004$ emu K mol^{-1} at 110 K, is obtained for the sample with the relative ratio 1.000 : 0.101 of the S = 1 state and S = ½ side-product at 110 K (Figure 4). The forbidden $|\Delta m_S| = 2$ transition displays a modest intensity (Figure 5A), which is consistent with a significant spectral width ($2D$ = 403 MHz) of the $|\Delta m_S| = 1$ region (Figure 4, Table 1).[50]

The relative orientations of ***D***-, ***A***-, and ***g***-tensors with respect to the plane of the dihydrophenazine moiety in **2²•**-C_2 are distinctly different from those for the previously reported S = 1 ground state **1²•²⁺**-D_2 and diradical **5** (Chart 1),[27,47,48] as summarized in Table 1.

Table 1. EPR parameters for triplet states of diradicals.[a]

Diradicals	D (MHz)	E (MHz)	$A_{YY}/2$ (MHz)	$A_{ZZ}/2$ (MHz)	g_{XX}	g_{YY}	g_{ZZ}
1²•²⁺-D_2	333	47	<4	22	2.0036	2.0035	2.0025
5	258	58	<2	30	2.0030	2.0043	2.0019
2²•-C_2	201	3.9	28	<2	2.0038	2.0026	2.0043
DFT[b]	–254	–32	+28	<1.2	2.0032	2.0024	2.0042
DFT[c]	–246	–21	+35	<0.9	2.0029	2.0024	2.0031

[a] Microwave frequencies (GHz), ν = 9.4387, 9.4645, and 9.2906 for diradicals **1²•²⁺**-D_2, **5** (Chart 1), and **2²•**-C_2, respectively; spectral simulations are performed with EasySpin.[50] [b,c] Computed with ORCA for **2²•**-C_2 at the B3LYP/EPR-II//UB3LYP-6-31G(d)+ZPVE (gas phase) and at the ωB97X-D3/EPR-II//UωB97XD/6-31G(d,p)/PCM-UFF+ZPVE (THF solvent model) level; see: SI, Table S5.5.[57,58]

Chart 1. Aminyl diradical **5**.

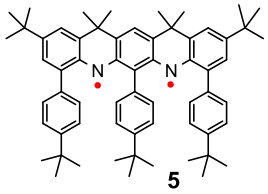

5

The *Y*-turning points (*Y*-lines) in the EPR spectrum of $\mathbf{2}^{2\bullet}$-C_2, which include the second outermost peaks (Figure 4A), are split into pentuplets with spacings of $|A_{YY}|/2$, where A_{YY} is the largest principal value of the ^{14}N hyperfine tensor (the ***A***-tensor) of two nitrogen nuclei. This is in contrast to the splitting of the two outermost peaks (*Z*-lines) with spacings of $|A_{ZZ}|/2$, where A_{ZZ} is the largest principal value of the ***A***-tensor of ^{14}N nuclei in diradicals $\mathbf{1}^{2\bullet 2+}$-D_2 and **5**, and in other related planar $S = 1$ aminyl diradicals.[27,46-48,51,52]

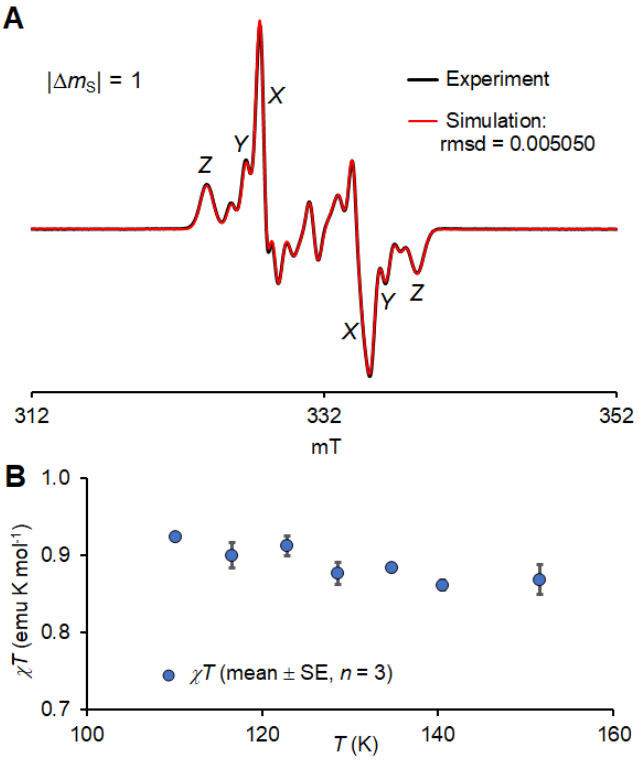

Figure 4. EPR (X-band) spectroscopy of 0.74 mM diradical *rac*-$\mathbf{2}^{2\bullet}$-C_2 in 2-MeTHF/toluene, 1 : 3.41. **A**: EPR (110 K, ν = 9.2906 GHz) spectrum ($|\Delta m_S| = 1$ region). Simulation (rmsd = 0.005050) using two components (states), $S = 1$ and $S = ½$, with the relative weights $w_1 : w_{1/2} = 1.000 : 0.101$. Center lines correspond to the $S = ½$ impurity. **B**: Quantitative EPR spectroscopy. At 110 K, $\chi T = 0.923 \pm 0.004$ (mean ± SE, $n = 3$) emu K mol^{-1}. For more details, including simulations of EPR spectra, see: Table 1 and SI: Table S3.1 and Figs. S1.58 and S1.60.

In *N*-centered π-radicals, the largest principal value of the ^{14}N hyperfine tensor is expected to coincide with the direction of the nitrogen $2p_\pi$ orbital.[53] Therefore, the $2p_\pi$ orbital in $\mathbf{2}^{2\bullet}$-C_2 can be considered to be approximately parallel to the *Y*-axis, which is the direction of the second largest principal value of the ***D***-tensor. Assuming that the ***D***-tensor primarily originates in the magnetic dipole–dipole interactions,[54-56] these relative orientations of ***D***- and ***A***-tensors in $\mathbf{2}^{2\bullet}$-C_2 suggest a "prolate-like" shape of spin density that is elongated in the direction of the *Z*-axis. This contrasts with an "oblate-like" shape of spin density in $\mathbf{1}^{2\bullet 2+}$-D_2 and diradical **5**, that is compressed in the direction of the *Z*-axis, which is parallel to the $2p_\pi$ orbitals. As expected for π-radicals, including aminyl radicals, the smallest principal value of the ***g***-tensor is parallel to the $2p_\pi$ orbitals, and thus coinciding with the direction of the largest principal value of the ***A***-tensor, such as g_{YY} in $\mathbf{2}^{2\bullet}$-C_2 and g_{ZZ} in $\mathbf{1}^{2\bullet 2+}$-D_2 and diradical **5**. Notably, the absolute values of D, $A_{YY}/2$, and g_{YY} are well reproduced by DFT-computations[56,57] for $\mathbf{2}^{2\bullet}$-C_2, except for the inherently-difficult- to-compute parameter E (Table 1 and *vide infra*).

The values of χT decrease with increasing T (Figure 4B), as expected for a triplet ground state with moderate value of singlet triplet energy gap, $\Delta E_{ST} = 2J/k \approx 100 - 300$ K. Nevertheless, the quantitative fit is not reliable because of the narrow temperature range available for a relatively polar matrix such as 2-MeTHF, and thus we carry out SQUID magnetometry for *rac*-$\mathbf{2}^{2\bullet}$-C_2 in 2-MeTHF matrix.

SQUID magnetometry. Using our custom-made EPR/SQUID tubes,[59,60] we prepared two samples of *rac*-$\mathbf{2}^{2\bullet}$-C_2 in 2-MeTHF and studied them by consecutive EPR spectroscopy and SQUID magnetometry.[49] For one of the samples, we adequately accounted for diamagnetism by strict point-by-point background subtraction. These studies unequivocally confirm the triplet ground state, as evidenced by the $S = 1$ paramagnetic behavior in both the magnetization (M) vs magnetic field (H) and the χT vs. T plots (Figure 5).

The M/M_{sat} vs H/T plots for *rac*-$\mathbf{2}^{2\bullet}$-C_2 at 1.8, 2, 3, and 5 K closely follow the $S = 1$ Brillouin function. The curvature of the plots, which does not depend on the radical concentration or the amount of sample, indicates that the measured $S \approx 1.0$ is the ground state. The magnetization at saturation, $M_{sat} = 0.80$ μ_B, in the Figure 5B plot indicates spin concentration of 80%, which agrees well with the mass factor, $w = 0.82$, obtained from the fits of the χT vs. T data. Both M_{sat} and w account for the EPR-determined content of $S = ½$ monoradical in Figure 5A, see: next paragraph.

The χT vs. T data were fit to a diradical-plus-monoradical model, in which molar fractions of paramagnetic $S = 1$ diradical (x_1) and $S = ½$ monoradical ($1 - x_1$) are fixed, based upon EPR spectra of the SQUID samples, e.g., Figure 5A. The fits involve two variable parameters: the singlet triplet energy gap, $2J/k$, and the mass factor, w, accounting for inaccuracies in mass balance. To account for very weak inter-molecular interactions (compared to $2J/k$) between diradical (and monoradical) molecules at low T, *i.e.* when the data extend down to $T = 1.8$ K, an additional variable, the mean-field parameter, θ(K), is utilized.

For two samples of *rac*-$\mathbf{2}^{2\bullet}$-C_2, the acquired six sets of data (mean ± SE, $n = 6$) provide the average values of $2J/k = 208 \pm 12$ K and $\Delta E_{ST} = 0.42 \pm 0.02$ kcal mol^{-1} (Figure 5 and SI).

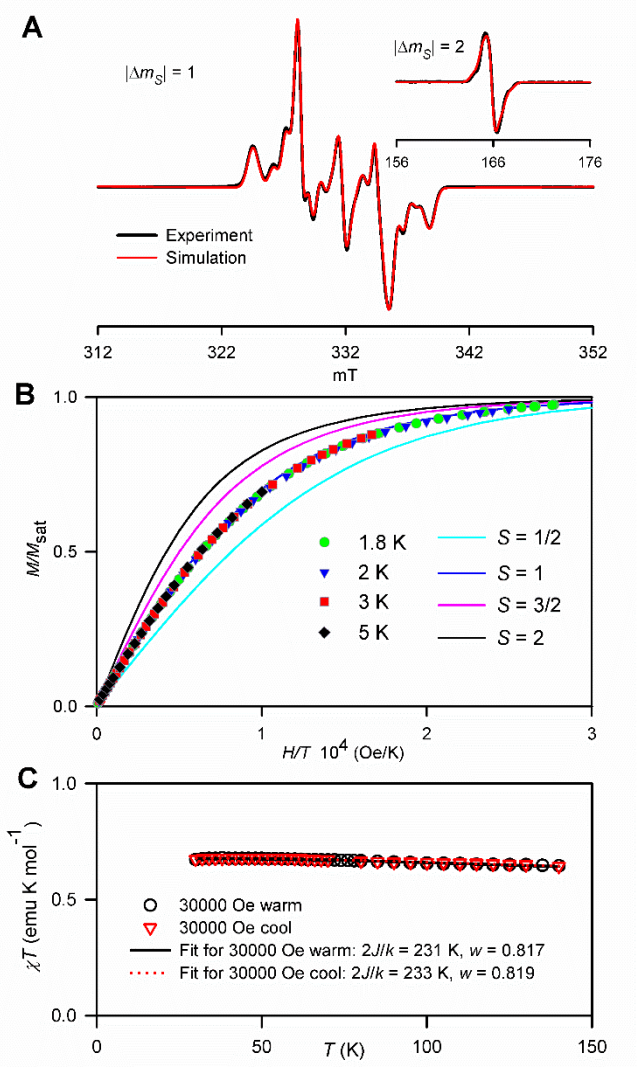

Figure 5. EPR/SQUID magnetic characterization of 25 mM diradical *rac*-**2²•**-C_2 in 2-MeTHF. **A**: EPR (X-band) spectrum in 2-MeTHF at 117 K after the SQUID magnetic studies. Inset plot: $|\Delta m_S| = 2$ region. Simulation of the $|\Delta m_S| = 1$ region, using two components (states) with $S = 1$ and $S = ½$, indicates their relative weights $w_1 : w_{1/2} = 1.000 : 0.402$. **B**: M/M_{sat} vs H/T plots, at T = 1.8–5 K (symbols) and the Brillouin curves corresponding to S = 1/2–2 (lines); $M_{sat} = 0.80\ \mu_B$. **C**: raw χT vs T data at H = 30000 Oe in the T = 30 – 140 K range were fit to a model, with molar fractions of diradical and monoradical fixed by the EPR spectra, using two variable parameters (Eq. S8, SI): singlet–triplet energy gap, $2J/k$ and mass factor, w. The values of variable parameters, mean ± standard error, parameter dependence, *DEP*, statistically adjusted coefficient of determination, R^2_{adj}, and standard error of estimate, *SEE* are as follows: in the warming mode, $2J/k = 231 \pm 3.1$ K, $w = 0.817 \pm 0.0006$, *DEP* = 0.717, R^2_{adj} = = 0.9712, *SEE* = 0.0018; in the cooling mode, $2J/k = 233 \pm 3.6$ K, $w = 0.819 \pm 0.0006$, *DEP* = 0.677, R^2_{adj} = 0.9662, SEE = 0.0019. Further details are reported in the SI: Tables S1.15 and S1.16, Figs. S1.85–S1.88, and Eq. S8.

UV-vis and ECD spectroscopy of tetraamine and its barrier for racemization. UV-vis and electronic circular dichroism (ECD) spectra for **2**-H_2-C_2 are shown in Figure 6. The double helical (*PP*)- and (*MM*)-enantiomers of neutral tetraamine are associated with negative and positive ECD couplets at the longest wavelength, respectively. This observation is confirmed by TD-DFT computations (Figure 6 and SI). The ECD spectrum with the negative couplet at the longest wavelength is invariably associated with the (*M*) and (*MM*) enantiomers of helical and double helical π-systems,[27,61] with many exceptions for double helical systems.[62-64] Notably, the enantiomer of neutral tetraamine (*PP*)-**2**-H_2-C_2 exhibits moderately strong chirooptical properties, as determined by the absorption anisotropy factor, $|g| = |\Delta\varepsilon|/\varepsilon = 0.036$ at λ = 376 nm (Figure 6). This factor is comparable to $|g| = 0.039$ and 0.035 reported for other double helices, carbon-sulfur and bis-perylene diimide[65,66] but smaller than $|g| = 0.052$ for expanded [23]helicene[67,68] and $|g| = 0.20$ for Zn(II)-helicate.[62,69]

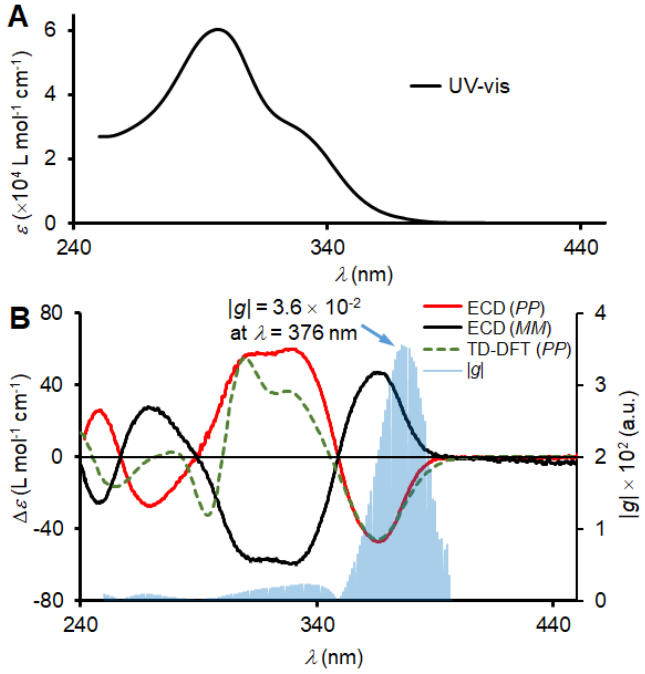

Figure 6. A: UV-vis absorption spectrum of tetraamine (*PP*)-**2**-H_2-C_2 in cyclohexane. **B**: ECD spectra of (*PP*)- and (*MM*)-**2**-H_2-C_2. in cyclohexane with a plot of anisotropy factor $|g| = |\Delta\varepsilon|/\varepsilon$ vs λ. TD-DFT computed ECD spectrum for (*PP*)-**2**-H_2-C_2. For further details, see: SI: Table S1.11, Figs. S1.73–S1.75.

The barrier for racemization of tetraamine (*MM*)-**2**-H_2-C_2 (%ee 94.4) is measured at 210, 230, and 250 °C, by using two solid samples at each temperature. Following heating for 1 – 56 h, the enantiomer-content for all six samples is analyzed by analytical SFC, showing decreased ee 88.6 – 79.4%. These data provide the barrier for racemization $\Delta G^‡ = 43.00 \pm 0.01$ kcal mol^{-1} in the 210 – 250 °C range (Table S2.1, SI). Because of the narrow temperature range, with three temperature data points, the data fitting to the linearized Eyring equation is not very reliable with respect to determination of $\Delta S^‡$, though statistically adjusted R^2 is 0.9998. The fit provides the following activation parameters: $\Delta H^‡ = 42.6 \pm 0.5$ kcal mol^{-1} and $\Delta S^‡ = -0.8 \pm 0.9$ cal mol^{-1} K^{-1}, i.e., practically, the entropy of activation, $\Delta S^‡ \approx 0$ cal mol^{-1} K^{-1}, is negligible (Table S2.2, SI). The free energy barrier, $\Delta G^‡ = 43.00 \pm 0.01$ kcal mol^{-1}, is comparable to $\Delta G^‡ = 42.4$ kcal mol^{-1} in all-phenylene [8]helicene,[70] or $\Delta G^‡ = 39.0 \pm 0.2$ kcal mol^{-1} in carbon-sulfur [7]helicene,[36] and it is much higher than $\Delta G^‡ = 24.1$ kcal mol^{-1} in all-phenylene [5]helicene, which racemizes at 298 K with a half-life of 50 min.[71,72]

Decay of diradical and monoradical. We monitor the decay of diradical (*MM*)-**2²•**-C_2 and related monoradical (*MM*)-**2•**-H-C_1 by

quantitative EPR spectroscopy, in conjunction with simulations of the spectra at each time point. The relative weights w_1 and $w_{1/2}$ for $S = 1$ and $S = 1/2$ states, obtained from simulations of EPR spectra, and values of χT (EPR), based on TEMPONE reference, are used to estimate the weight of diamagnetic tetraamine, w_0, from Eq. S3 (SI).[49] The resultant corrected molar fractions X_1, $X_{1/2}$, and X_0 at 117 K (Eq. S3, SI) are determined for $S = 1$ diradical, $S = ½$ monoradical, and diamagnetic tetraamine (including singlet excited state of diradical), respectively (Scheme 3, Figure 7).

The corrected molar fractions, $X_1 = A(t)$ and $X_{1/2} = B(t)$ for the diradical and monoradical (Scheme 3 and Eqs. S3A-C, SI), respectively, are then fit to the integrated kinetic equations (Eqs. S2A&B, SI). To minimize parameter dependence in each fit, we use only two variable parameters, the starting molar fraction and the rate constant (Figure 7 and Table S1.10, SI).

Scheme 3. Decay of $S = 1$ diradical: consecutive first order kinetics.

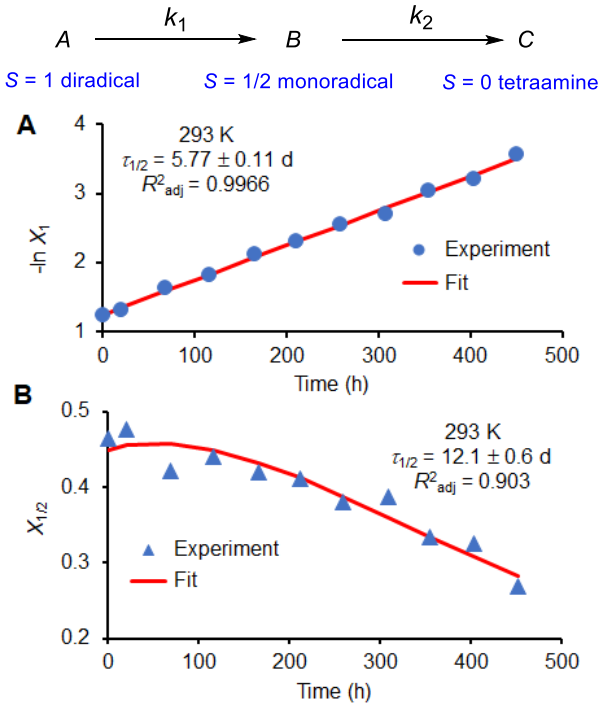

Figure 7. Decay kinetics of $S = 1$ diradical (*MM*)-**2²•**-C_2 (**A**) and $S = ½$ monoradical (*MM*)-**2•**-H-C_1 (**B**) in 2-MeTHF at 293 K. The data are from quantitative EPR spectroscopic monitoring at 117 K. Molar fractions X_1 and $X_{1/2}$, which are corrected for the presence of diamagnetic tetraamine products and $S = 0$ excited state of diradical, correspond to $S = 1$ diradical and $S = ½$ monoradical, respectively. Fits are based on the Scheme 3 (above), using Eqs. S2A&B, SI. More details may be found in the SI: Eqs. S3A-C, Tables S1.5, S1.6, and S1.10, Figs. S1.62–1.64, and S1.66.

For diradical (*MM*)-**2²•**-C_2 and monoradical (*MM*)-**2•**-H-C_1, half-lives $\tau_{1/2} = 5.8 \pm 0.1$ d and $\tau_{1/2} = 12.1 \pm 0.6$ d are obtained and the anticipated $k_1 > k_2$ is observed.[47,49] Similar to the decay of aminyl triradical,[49] when fitting the double integrated intensity (*DI*) of the diradical *Z*-line (instead of $X_1 = A(t)$), a somewhat inflated $\tau_{1/2} = 9.0 \pm 0.6$ d is obtained for the identical sample of (*MM*)-**2²•**-C_2 (Fig. S1.63A, SI); for comparison, an analogous fit for the best sample of enantiomer (*PP*)-**2²•**-C_2 gives a much shorter $\tau_{1/2} = 3.1 \pm 0.3$ d (Fig. S1.63B, SI). For these two samples after ca. 1 day at room temperature, relative contents of $S = 1$ diradical vs $S = ½$ monoradical are 1 : 1.78 (*MM*) and 1 : 1.21 (*PP*), based on simulations of their EPR spectra (Tables S1.5 and S4.1, SI).

We note that the $\tau_{1/2}$ values of the diradical correlate with its relative content (vs. monoradical) in the sample at the initial time point, i.e., a higher content corresponds to a shorter half-life. This is perhaps best illustrated by the decay kinetics of various samples of *rac*-**2²•**-C_2 (e.g., Table 1.10, SI). In particular, the sample with a large diradical-to-monoradical ratio in Figure 4, shows a much shorter $\tau_{1/2} = 0.019 – 0.060$ d, as determined from $-\ln X_1$ vs. time data. It should be noted that values of $\tau_{1/2}$ are very approximate in such samples, especially in the initial stages of the decay. We postulate that these shorter $\tau_{1/2}$ imply faster reactions of aminyl diradical with excess of I_2 that is required to attain a high yield of diradical, analogous to that found for recently studied aminyl triradical.[49]

The spectrum of monoradical *rac*-**2•**-H-C_1 at 293 K, featuring $g = 2.0030$ and well resolved one-nucleus hyperfine couplings, $A(^{14}N) = 20.5$ MHz and $A(^1H) = 8.46$ MHz, is observed toward the very end of the decay of racemic diradical (Fig. 1.70, SI).

The previously reported diradical **5** (Chart 1) and corresponding monoradical, which are devoid of excess of iodine, possess $\tau_{1/2} = 2.83 \pm 0.03$ h and 6.57 ± 0.03 h in 2-MeTHF at room temperature, as determined by EPR spectroscopic monitoring.[47] Similarly, for more spin-dilute, triphenylene-based aminyl diradical and monoradical, $\tau_{1/2} = 12.8 \pm 0.4$ h and 18.3 ± 0.8 h are found.[49] With half-life of up to a few days, (*MM*)-**2²•**-C_2 is distinctly the most persistent high-spin aminyl diradical to date.

UV-vis-NIR and ECD spectroscopy. We first obtain ECD spectra of enantiomers of diradical at 274 K (Figure 8).

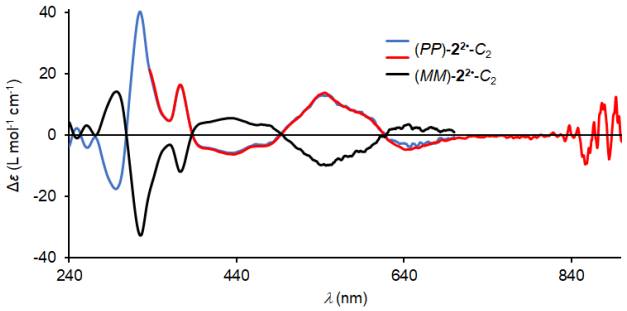

Figure 8. Initial ECD spectra of 0.32 mM (*PP*)-**2²•**-C_2 and 0.29 mM (*MM*)-**2²•**-C_2 in 2-MeTHF at 274 K, prior to sample warm up to room temperature (293 K). More details may be found in Table S1.11 and Fig. S1.76, SI.

We note that the spectra (Figure 8) are not exact mirror images because of different %ee of the precursor tetraamine and sample-dependent efficiency for the generation of diradicals, as well as the approximate concentrations of diradicals.

After warming up to room temperature, the samples are studied by both EPR spectroscopy (preceding section) and UV-vis-NIR and ECD spectroscopy (Figure 9). Notably, the initial ECD spectra at room temperature of both enantiomers show minor changes in intensities from the initial spectra at 274 K (SI).

The decay of spectral intensity in Figures 9A and 9D appears to be on a qualitatively similar time scale as in EPR spectroscopy (Figure 7). Because the EPR, ECD, and UV-vis-NIR spectra are obtained within 2 – 3 hrs, we can use the EPR-derived molar fractions to extract the ECD and UV-vis-NIR spectra for the pure diradical and monoradical (Eqs. S5A&B, SI). The extracted spectra shown in Figures 9B, C, E, and F are reasonably reproduced by TD-DFT

computations (see below: DFT computations section); also, as observed for (*MM*)-tetraamine, the longest wavelength ECD absorption computed by TD-DFT corresponds to a positive sign of $\Delta\varepsilon$ for the (*MM*)-enantiomer of diradical (Figure 9D).

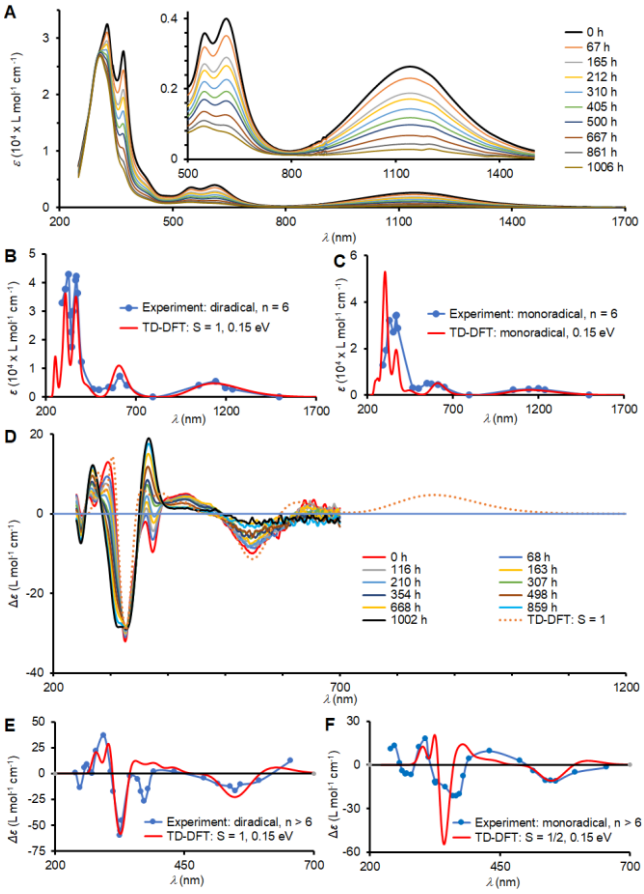

Figure 9. UV-vis-NIR absorption spectra (**A** – **C**) and ECD spectra (**D** – **F**) of diradical (*MM*)-**2²•**-C_2 and S = ½ monoradical (*MM*)-**2•**-H-C_1 in 2-MeTHF at 293 K. UV-vis-NIR (**A**) and ECD (**D**) spectra for (*MM*)-**2²•**-C_2 after annealing for 0 – 1000 h at 293 K. Derived spectra for (*MM*)-**2²•**-C_2 (**B** and **E**) and (*MM*)-**2•**-H-C_1 (**C** and **F**), together with TD-DFT computed spectra for S = 1 (*MM*)-**2²•**-C_2 and S = ½ (*MM*)-**2•**-H-C_1 at the UωB97XD/6-31G(d,p)/IEF-PCM-UFF+ZPVE (in THF) level of theory.

The diradical possesses considerably more intense ECD spectra, compared to the monoradical. This is reflected by absorption anisotropy factors, $|g| \approx 0.0048$ at 548 nm and $|g| \approx 0.0022$ at 539 nm, for the diradical and monoradical, respectively (Figs. S1.82 and S1.83, SI). For comparison, triplet ground state diradical dication (*M*,*M*)-**1²•²⁺**-2SbF_6^- in dibutylphthalate has similar $|g| = 0.005$ at 385 nm[27] and various singlet ground state *N*-centered biradical dications have the range of $|g|$ from 0.001 at 920 nm to 0.0046 at 652 nm.[14,15,19] In addition, $|g| = 0.0038$ at 316 nm was reported for porphyrin-[6]helicene-based C-centered S = ½ radical.[11]

Estimates of the racemization barrier for diradical. The conversion of tetraamine to aminyl diradical, corresponds to the loss of two hydrogen atoms positioned at inner parts of the [5]helicene-like moieties. Therefore, a significant decrease of the racemization barrier in (*MM*)-**2²•**-C_2 may be expected.

We isolated tetraamine (*MM*)-**2**-H_2-C_2 in 75% yield as the final product after the EPR/UV-vis-NIR/ECD spectroscopic monitoring experiments (Figures 7 and 9). Notably its %ee has decreased from the initial value of 94.2 to a value of 86.2. Based on these values, and assuming total time equal to half-life of 5.8 d for the diradical, the barrier for racemization of (*MM*)-**2²•**-C_2 is estimated as $\Delta G^{\ddagger} \approx$ 26.6 kcal mol^{-1}, which may be viewed as an approximate lower limit of ≥26 kcal mol^{-1}.

Notably, this value is comparable to the racemization barrier for (*MM*)-**2²•**-C_2, $\Delta G^{\ddagger} \approx 26$ kcal mol^{-1}, determined by considering a difference in first order rate constants obtained by ECD vs UV-vis spectral monitoring of the diradical decay (SI, Section 1e, Fig. S1.77). For comparison, [4]helicene-based aminyl radical, possessing two sterically encumbered methoxy groups (Figure 1), racemizes with $\Delta G^{\ddagger} = 26.7$ kcal mol^{-1}.[4]

DFT computations. All DFT geometry optimizations and TD-DFT computations are carried out with Gaussian 16.[58] EPR spectral parameters for radicals were computed by ORCA.[57]

Barriers for racemization: Barriers for racemizations of (*MM*)-**2²•**-C_2 and tetraamine (*PP*)-**2**-H_2-C_2 are computed at the UB3LYP/6-31G(d,p)+ZPVE (gas phase) and RωB97XD/6-31G(d,p)/IEF-PCM-UFF+ZPVE (cyclohexane) level of theory,[73] respectively. The free energy ($\Delta G°$ at 298 K) surface for racemization of (*MM*)-**2²•**-C_2 consists of two enantiomeric C_2-symmetric global minima, two enantiomeric C_1-symmetric transition states and a C_i-symmetric, *meso* intermediate (Figure 10 and Fig. S5.1, SI).

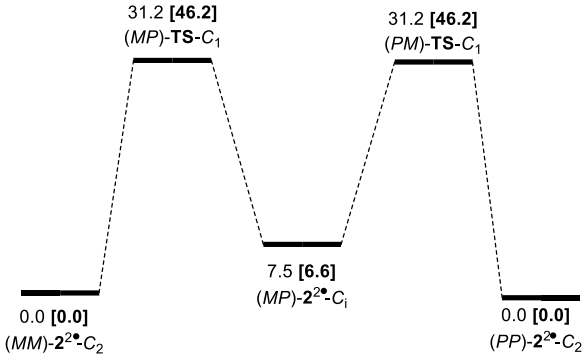

Figure 10. Free energy ($\Delta G°$ at 298 K) surface for racemization of the triplet state of aminyl diradical **2²•**-C_2 at the UB3LYP/6-31G(d,p)+ZPVE level of theory; in brackets, values of $\Delta G°$ at 500 K for racemization of tetraamine **2**-H_2-C_2 at the RωB97xD/6-31G(d,p)/IEF-PCM-UFF+ZPVE (in cyclohexane) are given.

An analogous surface is found for tetraamine. The free energies, $\Delta G°$, for the global minima are 7.5 kcal mol^{-1} (diradical) and 6.6 kcal mol^{-1} (tetraamine) below the C_i-symmetric *meso* intermediates (*MP*). However, the C_1-symmetric enantiomeric transition states, (*MP*) and (*PM*), are $\Delta G^{\ddagger} = 31.2$ kcal mol^{-1} (diradical) and $\Delta G^{\ddagger} = 46.2$ kcal mol^{-1} (tetraamine) above the global minima. These DFT-computed values of $\Delta G^{\ddagger}$ compare well with the experimentally determined lower limit of $\Delta G^{\ddagger} \geq 26$ kcal mol^{-1} for the diradical and measured $\Delta G^{\ddagger} = 43.00 \pm 0.01$ kcal mol^{-1} for the tetraamine.

Singlet-triplet energy gaps: The energy gaps, ΔE_{ST}, corrected for spin contamination (Eq. S9, SI),[74,75] are computed at the UB3LYP/6-31G(d,p)+ZPVE level of theory. Values of $\Delta E_{ST} = 0.67$, 0.89, and 1.38 kcal mol^{-1} are obtained for **2²•**-C_2, **2²•**-C_i, and the transition state for racemization, respectively. As expected for this level of theory, the computed value for the ground state triplet C_2-symmetric diradical is somewhat overestimated,[75-78] compared to the experimental $\Delta E_{ST} = 0.42 \pm 0.02$ kcal mol^{-1}.

Electronic absorption spectra: UV-vis-NIR and ECD absorption spectra for tetraamine (*MM*)-, (*PP*)-**2**-H$_2$-C_2, S = 1 diradical (*MM*)-, (*PP*)-**2²•**-C_2 and S = ½ monoradical (*MM*)-, (*PP*)-**2•**-H-C_1 were obtained by TD-DFT computations. The computations of the diamagnetic species are carried out in cyclohexane or dichloromethane solvent models at the RωB97XD/6-31G(d,p)/IEF-PCM-UFF+ZPVE level, while the paramagnetic species in THF solvent model are at the UωB97XD/6-31G(d,p)/IEF-PCM-UFF+ZPVE level of theory. At the longest wavelength, an intense transition with a sign opposite to that for the helicity is obtained, i.e., negative for (*PP*)- and positive for (*MM*)-enantiomers (Figures 6B and 9D, Table S5.2, SI).

Notably, this inverted sign for the longest wavelength ECD transition is also found for tetraamine (*PP*)-**2**-H$_2$-C_2 and its single helix model compound (*P*)-**6**-C_1 in a cyclohexane solvent model at the RCAM-B3LYP/6-31G(d,p)/IEF-PCM-UFF and RωB97XD/6-31G(d,p)/IEF-PCM-UFF+ZPVE levels (Table S5.2, SI). For the triplet ground state of diradical (*PP*)-**2²•**-C_2, there are two longest wavelength transitions at λ = 778 and 753 nm with relative rotatory strengths, R (length) = +9.8 and –56.3, respectively (Table S5.2, SI); consequently, in Figure 9D, the peak at λ = 753 nm dominates as the longest wavelength transition, after Gaussian broadening. For monoradical (*PP*)-**2•**-H-C_1, a single, well separated, longest wavelength transition at λ = 760 nm with relative rotatory strength, R (length) = –21.2, is found (Table S5.2, SI).

EPR spectral parameters: EPR parameters for S = 1 state of diradical (*MM*)-**2²•**-C_2 are computed at the B3LYP/EPR-II//UB3LYP-6-31G(d)+ZPVE (gas phase) and the ωB97X-D3/EPR-II//UωB97XD/6-31G(d,p)/PCM-UFF+ZPVE (THF solvent model) levels; both computations give a reasonable agreement with the experiment (Table 1). In particular, the orientations of ***D***-, ***A***-, and ***g***-tensors are in perfect agreement with the experiment. Values of $|D|$ for aminyl diradicals (and triradicals) are typically overestimated by about 100%, compared to the experiment.[48,51,52] However, for **2²•**-C_2, the computed values of $|D|$ are overestimated by about 25%, similarly to that for aminium diradical dication **1²•²⁺**-D_2-2SbF$_6^-$.[27] Also, we note that the ^{14}N-hyperfine splitting, $|A_{YY}|/2$, of the Y-line pentuplets in **2²•**-C_2 is perfectly reproduced at the B3LYP/EPR-II level and a bit overestimated at the ωB97X-D3/EPR-II level (Table 1). For monoradical **2•**-H-C_1, computed at the ωB97X-D3/EPR-II level, isotropic ^{14}N- and ^{1}H- hyperfine splittings, A_{iso} = 24.4 and –12.7 MHz, are somewhat overestimated, compared to the corresponding experimental values (absolute values) of 20.5 and 8.46 MHz. The computed EPR g-value, g_{iso} = 2.0028 is found to be in good agreement with experimental g = 2.0030 (Tables S5.5 and S5.6, SI).

Aminyl radical anions and SOMO/HOMO inversion: The aminyl radical anion **2•⁻**-C_1, the intermediate in the I_2-mediated oxidation of dianion to aminyl diradical **2²•**-C_2 (Scheme 2), is a one-electron reduced species that is related to the high-spin diradical. Thus, it has potential to display SOMO/HOMO energy level inversion (SHI).[1,79-82]

We have recently defined two quantitative measures of SHI:[1]

$$SHI = [(\alpha\text{-HOMO} + \beta\text{-HOMO})/2] - \alpha\text{-SOMO} \quad (1)$$

$$\alpha SHI = \alpha\text{-HOMO} - \alpha\text{-SOMO} \quad (2)$$

SHI, as expressed in Eq. 1, is the difference in energy of electrons in HOMO (average of α-MO and β-MO) vs. SOMO (α-MO); i.e., SHI > 0 implies that the energy of the SOMO is below the energy of the HOMO on a per electron basis. As described in Eq. 2, αSHI > 0 corresponds to a conventional, more restrictive definition of SOMO/HOMO inversion. We prefer to use SHI because it is expressed on per electron basis, and typically shows a good linear correlation with ΔE_{ST} in the corresponding diradicals.[1]

We carry out a geometry optimization of radical anion (*PP*)-**2•⁻** at the UB3LYP/6-31+G(d,p)+ZPVE level of theory, starting with the C_2-symmetric triplet geometry of the (*PP*)-diradical, to produce the **2•⁻**-C_2 structure that possesses a stable wave function. Spin density in the radical anion structure is distributed equally over the two aminyl nitrogens (Figure 11A), and values of SHI = 7.52 kcal mol^{-1} and αSHI = 0.59 kcal mol^{-1} are obtained.[1]

An analogous geometry optimization of radical anion (*PP*)-**2•⁻** at the UωB97xD/6-31G(d,p)/IEF-PCM-UFF+ZPVE (THF) level provides a C_2-symmetric minimum (SHI = 12.8 kcal mol^{-1}). However, its wave function is unstable, with respect to symmetry breaking to the C_1 point group. Re-optimization of this structure, gives a C_1-symmetric minimum of radical anion (SHI = 37.1 kcal mol^{-1}); further re-optimization, utilizing the 6-31+G(d,p) basis set, provides the final C_1-symmetric structure with SHI = 35.4 kcal mol^{-1} and αSHI = 35.2 kcal mol^{-1} (Figure 11B&C). Both C_1-symmetric structures possess a spin density that is unequally distributed over the two aminyl nitrogens, as illustrated for one of them in Figure 11B. We note that this large SHI is comparable to SHI = 27 – 41 kcal mol^{-1} computed in radical anions derived from various nitronyl nitroxide- or oxo-verdazyl-based high-spin diradicals – all possessing multiple (from 2 to 4) three-electron bonds within their π-systems.[1]

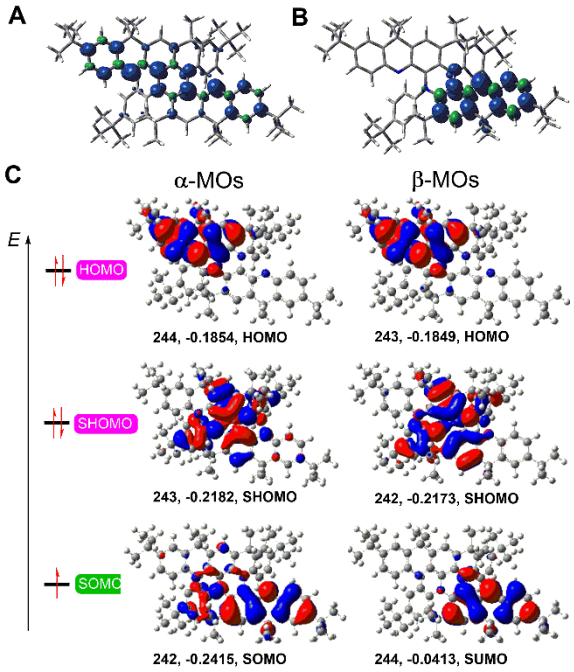

Figure 11. DFT computations for aminyl radical anion (*PP*)-**2•⁻**. Spin density distributions, are shown at the iso-density level of 0.002 electron/Bohr^3, for **2•⁻**-C_2 at the UB3LYP/6-31+G(d,p) (gas phase) level (**A**) and **2•⁻**-C_1 at the UωB97xD/6-31+G(d,p)/IEF-PCM-UFF (THF) level (**B**). Orbital maps for the C_1-symmetric structure of the radical anion, shown above. Positive (red) and negative (blue) contributions are displayed at the isodensity level of 0.02 electron/Bohr^3 (**C**). Additional data may be found in the SI: Tables S5.3 and S5.4.

CONCLUSION

We have prepared the first high-spin (S = 1) neutral diradical, with delocalized spin density within an enantiomerically enriched helical π-system. The unusual spin density distribution in the diradical,

which embodies two 3-electron C-N bonds, is correlated with its triplet ground state and excellent persistence at room temperature. We postulate that the presence of two 3-electron bonds in the corresponding diradical with relatively low ΔE_{ST}, may contribute to the computed large SOMO-HOMO inversion of ca. 35 kcal mol^{-1} in aminyl radical anion **2**$^{\bullet-}$-C_1.

EXPERIMENTAL SECTION

Synthesis, resolution of *rac*-**2**-H_2-C_2 with chiral auxiliary, and DFT computations are described in detail in the SI.

X-ray Crystallography of Tetraamine *rac*-2-H_2-C_2

Crystals of *rac*-**2**-H_2-C_2 were obtained by sublimation at 350 °C. Data were collected at 130 K using Mo Kα radiation and integrated (SAINT).[83] Intensity data were corrected for absorption.[84] Space group C_2/c was determined based on intensity statistics and systematic absences. The structure was solved with intrinsic methods and refined on F^2 using SHELX suite of programs.[85,86] Crystal data are as follows: $C_{64}H_{76}N_4$, M_r = 901.29 g mol^{-1}, colorless/violet block, 0.20 × 0.10 × 0.10 mm^3, monoclinic, C_2/c, μ(*Mo K*α) = 0.061 mm^{-1}, ϑ_{max} = 26.40°, 77,980 reflections measured, 11,528 independent (R_{int} = 0.0566), $R1$ = 0.0454 [$I > 2\sigma(I)$], $wR2$ = 0.1287 (all data), goodness of fit on F^2: 1.011, residual density peaks: 0.338 and −0.230 e Å^{-3}. The remaining electron density is in the vicinity of the three disordered *t*-butyl groups. The structure features potential solvent accessible voids of 1128 Å^3 per unit cell with no significant electron density (<0.2 e Å^{-3}).[87] Additional crystal and structure refinement data for *rac*-**2**-H_2-C_2 are in the Supporting Information and the file in CIF format, deposited to CCDC.

SFC

Resolution of tetraamine *rac*-**2**-H_2-C_2, using SFC on a preparative scale, is implemented with Teledyne LABS ACCQPrep SFC instrument, equipped with ChromegaChiral prep column (CCO, 5-μ, 20 mm x 250 mm). The instrument allows for efficient, automated stacked injections, which were necessary due to the limited solubility of the compounds. Total instrument time required to resolve 50-mg sample of *rac*-**2**-H_2-C_2, including fraction recycling, was about 8 hours. Enantiomeric excesses of samples (and fractions) from resolutions by chiral auxiliary (and by SFC) were analyzed with Agilent 1260 Infinity SFC, equipped with a ChromegaChiral-column (CCO, 5-μ, 4.6 mm x 150 mm). Values of %ee were derived from BiGaussian fits.

EPR Spectroscopy and SQUID Magnetometry

CW EPR spectra (X-band) are obtained on a Bruker EMX+ equipped with a Bruker high-sensitivity cavity (Figures 4, 5, and 7). The samples of **2**$^{2\bullet}$-C_2 in 2-MeTHF (or 2-MeTHF/toluene) are typically enclosed in a 4- or 5-mm O.D. EPR tubes fused to a high-vacuum Kontes stopcock with solv-seal joint. The spectra are simulated with EasySpin, using either *pepper* or *garlic* modules.[50]

Magnetic data (Figure 5) are acquired using SQUID magnetometer (MPMS-5S/XL). Samples of 19 and 25 mM *rac*-**2**$^{2\bullet}$-C_2 in 2-MeTHF were flamed-sealed in our custom-made EPR/SQUID tubes; the 5-mm O.D. tubes (thin wall EPR-quality quartz) contain a thin and flat "false bottom" ca. 5 – 6 cm from the end of the tube.[59,60] The tubes are attached with heat-shrink tubing to the modified sample rod, and then transferred rapidly from liquid nitrogen to the sample chamber of the magnetometer at 10 K, under helium atmosphere. To obtain values of ΔE_{ST}, the χT *vs* T data are numerically fit to Eq. S8 (SI), which also accounts for paramagnetic saturation effects at low temperatures.[88] More details may be found in the SI.

UV-vis-NIR and ECD Spectroscopy

UV-vis-NIR and ECD absorption spectra of enantiomerically enriched diradicals in 2-MeTHF are obtained in custom-made Schlenk vessels (containing 1-mm or 2-mm path-length quartz cuvette); one of the Schlenk vessels also included 4-mm O.D. EPR tube. In a typical set of experiments, ECD spectra of enantiomerically-enriched diradical are initially acquired at 274 K, which are then followed by the UV-vis-NIR, ECD, and EPR spectra at room temperature.

ASSOCIATED CONTENT

Supporting Information

The Supporting Information is available free of charge at https://pubs.acs.org/doi/xxxxxxxxxxx.
General procedures and materials, additional experimental and computational details.

Accession Codes

CCDC 2331114 contains the supplementary crystallographic data for this paper. These data can be obtained free of charge via www.ccdc.cam.ac.uk/data_request/cif, or by emailing data_request@ccdc.cam.ac.uk, or by contacting The Cambridge Crystallographic Data Centre, 12 Union Road, Cambridge CB2 1EZ, UK; fax: +44 1223 336033.

Terms & Conditions

AUTHOR INFORMATION

* Corresponding Author
arajca1@unl.edu

Notes

The authors declare no competing financial interests.

ACKNOWLEDGMENT

We thank the NSF Chemistry Division for support of this research under Grants CHE-1955349 and CHE-2247170. Support for the acquisition of the Bruker Venture D8 diffractometer through the Major Scientific Research Equipment Fund from the President of Indiana University and the Office of the Vice President for Research is gratefully acknowledged. We thank Drs. Kouichi Shiraishi and Przemysław J. Boratyński for their contributions to the preliminary syntheses of racemic tetraamine. We thank Professor Alexander Sinitskii (Chemistry at Nebraska) for the access to the UV–vis–NIR spectrophotometer.

‡ Current address: Dr. Chan Shu, Toyota Research Institute of North America, 1555 Woodridge Avenue, Ann Arbor, Michigan 48105, United States.

REFERENCES

(1) Shu, C.; Yang, Z.; Rajca, A. From Stable Radicals to Thermally Robust High-Spin Diradicals and Triradicals. *Chem. Rev.* **2023**, *123*, 11954–12003.

(2) Datta, S. N.; Pal, A. K.; Panda, A. Design of Magnetic Organic Molecules and Organic Magnets: Experiment, Theory and Computation with Application and Recent Advances. *Chem. Phys. Impact* **2023**, *7*, 100379. DOI: https://doi.org/10.1016/j.chphi.2023.100379

(3) Yeo, H.; Debnath, S.; Krishnan, B. P.; Boudouris, B. W. Radical polymers in optoelectronic and spintronic applications. *RSC Appl. Polym.* **2024**, *2*, 7–25. DOI: https://doi.org/10.1039/D3LP00213F

(4) Ueda, A.; Wasa, H.; Suzuki, S.; Okada, K.; Sato, K.; Takui, T.; Morita, Y. Chiral Stable Phenalenyl Radical: Synthesis, Electronic-Spin Structure, and Optical Properties of [4]Helicene-Structured Diazaphenalenyl. *Angew. Chem., Int. Ed.* **2012**, *51*, 6691–6695.

(5) Wang, Y.; Zhang, H.; Pink, M.; Olankitwanit, A.; Rajca, S.; Rajca, A. Radical Cation and Neutral Radical of Aza-thia[7]helicene with SOMO–HOMO Energy Level Inversion. *J. Am. Chem. Soc.* **2016**, *138*, 7298–7304.

(6) Zak, J. K.; Miyasaka, M.; Rajca, S.; Lapkowski, M.; Rajca, A. Radical Cation of Helical, Cross-Conjugated β-Oligothiophene. *J. Am. Chem. Soc.* **2010**, *132*, 3246–3247.

(7) Sørensen, T. J.; Nielsen, M. F.; Laursen, B. W. Synthesis and Stability of *N*,*N*′-Dialkyl-1,13-dimethoxyquinacridinium ($DMQA^+$): A [4]Helicene with Multiple Redox States. *ChemPlusChem* **2014**, *79*, 1030–1035. DOI: 10.1002/cplu.201402058

(8) Liu, J.; Ravat, P.; Wagner, M.; Baumgarten, M.; Feng, X.; Müllen, K. Tetrabenzo[a,f,j,o]perylene: A Polycyclic Aromatic Hydrocarbon With An Open-Shell Singlet Biradical Ground State. *Angew. Chem., Int. Ed.* **2015**, *54*, 12442–12446.

(9) Ravat, P.; Šolomek, T.; Rickhaus, M.; Häussinger, D.; Neuburger, M.; Baumgarten, M.; Juríček, M. Cethrene: A Helically Chiral Biradicaloid Isomer of Heptazethrene. *Angew. Chem., Int. Ed.* **2016**, *55*, 1183–1186.

(10) Ravat, P.; Ribar, P.; Rickhaus, M.; Häussinger, D.; Neuburger, M.; Juríček, M. Spin-Delocalization in a Helical Open-Shell Hydrocarbon. *J. Org. Chem.* **2016**, *81*, 12303–12317.

(11) Kato, K.; Furukawa, K.; Mori, T.; Osuka, A. Porphyrin-Based Air-Stable Helical Radicals. *Chem. Eur. J.* **2018**, *24*, 572–575.

(12) Narita, M.; Teraoka, T.; Murafuji, T.; Shiota, Y.; Yoshizawa, K.; Mori, S.; Uno, H.; Kanegawa, S.; Sato, O.; Goto, K.; Tani, F. An Azulene-Based Chiral Helicene and Its Air-Stable Cation Radical. *Bull. Chem. Soc. Jpn.* **2019**, *92*, 1867–1873.

(13) Tani, F.; Narita, M.; Murafuji, T. Helicene Radicals: Molecules Bearing a Combination of Helical Chirality and Unpaired Electron Spin. *ChemPlusChem* **2020**, *85*, 2093–2104. https://doi.org/10.1002/cplu.202000452

(14) Kasemthaveechok, S.; Abella, L.; Jean, M.; Cordier, M.; Roisnel, T.; Vanthuyne, N.; Guizouarn, T.; Cador, O.; Autschbach, J.; Crassous, J. Axially and Helically Chiral Cationic Radical Bicarbazoles: SOMO-HOMO Level Inversion and Chirality Impact on the Stability of Mono- and Diradical Cations. *J. Am. Chem. Soc.* **2020**, *142*, 20409–20418. DOI: 10.1021/jacs.0c08948

(15) Kasemthaveechok, S.; Abella, L.; Jean, M.; Cordier, M.; Vanthuyne, N.; Guizouarn, T.; Cador, O.; Autschbach, J.; Crassous, J.; Favereau, L. Carbazole Isomerism in Helical Radical Cations: Spin Delocalization and SOMO–HOMO Level Inversion in the Diradical State. *J. Am. Chem. Soc.* **2022**, *144*, 7253–7263. DOI: 10.1021/jacs.2c00331

(16) Chang, H.; Liu, H.; Dmitrieva, E.; Chen, Q.; Ma, J.; He, P.; Liu, P.; Popov, A. A.; Cao, X.-Y.; Wang, X-Y.; Zou, Y.; Narita, A.; Müllen, K.; Peng, H.; Hu, Y. Furan-containing double tetraoxa[7]helicene and its radical cation. *Chem. Comm.* **2020**, *56*, 15181–15184. DOI: https://doi.org/10.1039/D0CC06970A

(17) Rajca, A.; Shu, C.; Zhang, H.; Zhang, S.; Wang, H.; Rajca, S. Thiophene-Based Double Helices: Radical Cations with SOMO-HOMO Energy Level Inversion. *Photochem. Photobiol.* **2021**, *97*, 1376–1390. DOI: 10.1111/php.13475

(18) Li, C.; Zhang, C.; Li, P.; Jia, Y.; Duan, J.; Liu, M.; Zhang, N.; Chen, P. Red Emissive Double Aza[7]helicenes with Antiaromaticity / Aromaticity Switching via the Redox-Induced Radical Cation and Dication Species. *Angew. Chem. Int. Ed.* **2023**, *62*, e202302019. DOI: https://doi.org/10.1002/anie.202302019

(19) Zhao, F.; Zhao, J.; Liu, H.; Wang, Y.; Duan, J.; Li, C.; Di, J.; Zhang, N.; Zheng, X.; Chen, P. Synthesis of π-Conjugated Chiral Organoborane Macrocycles with Blue to Near-Infrared Emissions and the Diradical Character of Cations. *J. Am. Chem. Soc.* **2023**, *145*, 10092–10103.

(20) Naaman, R.; Paltiel, Y.; Waldeck, D. H. Chiral molecules and the electron spin. *Nat. Rev. Chem.* **2019**, *3*, 250–260.

(21) Kiran, V.; Mathew, S. P.; Cohen, S. R.; Hernandez Delgado, I.; Lacour, J.; Naaman, R. Helicenes—A New Class of Organic Spin Filter. *Adv. Mater.* **2016**, *28*, 1957–1962.

(22) Kettner, M.; Maslyuk, V. V.; Nürenberg, D.; Seibel, J.; Gutierrez, R.; Cuniberti, G.; Ernst, K.-H.; Zacharias, H. Chirality-Dependent Electron Spin Filtering by Molecular Monolayers of Helicenes. *J. Phys. Chem. Lett.* **2018**, *9*, 2025–2030.

(23) Rodríguez, R.; Naranjo, C.; Kumar, A.; Paola Matozzo, P.; Das, T. K.; Zhu, Q.; Vanthuyne, N.; Gómez, R.; Ron Naaman, R.; Sánchez, L.; Crassous, J. Mutual Monomer Orientation To Bias the Supramolecular Polymerization of [6]Helicenes and the Resulting Circularly Polarized Light and Spin Filtering Properties. *J. Am. Chem. Soc.* **2022**, *144*, 7709–7719. DOI: https://doi.org/10.1021/jacs.2c00556

(24) Shil, S.; Bhattacharya, D.; Misra, A.; Klein, D. J. A high-spin organic diradical as a spin filter. *Phys. Chem. Chem. Phys.* **2015**, *17*, 23378–23383.

(25) Cho, D.; Lee, J. Y. Organic Stable Radical Oligomers as Spin Filters. *J. Phys. Chem. C* **2023**, *127*, 8256−8262. DOI: https://doi.org/10.1021/acs.jpcc.3c00179

(26) Tahir, H.; Eedugurala, N.; Hsu, S.-N.; Mahalingavelar, P.; Savoie, B. M.; Boudouris, B. W.; Azoulay, J. D. Large Room-Temperature Magnetoresistance in a High-Spin Donor–Acceptor Conjugated Polymer. *Adv. Mater.* **2024**, *36*, 2306389. DOI: https://doi.org/10.1002/adma.202306389

(27) Shu, C.; Zhang, H.; Olankitwanit, A.; Rajca, S.; Rajca, A. High-Spin Diradical Dication of Chiral π-Conjugated Double Helical Molecule. *J. Am. Chem. Soc.* **2019**, *141*, 17287–17294. DOI: 10.1021/jacs.9b08711

(28) Gallagher, N. M.; Bauer, J. J.; Pink, M.; Rajca, S.; Rajca, A. High-Spin Organic Diradical with Robust Stability. *J. Am. Chem. Soc.* **2016**, *138*, 9377–9380.

(29) Gallagher, N.; Zhang, H.; Junghoefer, T.; Giangrisostomi, E.; Ovsyannikov, R.; Pink, M.; Rajca, S.; Casu, M. B.; Rajca, A. Thermally and Magnetically Robust Triplet Ground State Diradical. *J. Am. Chem. Soc.* **2019**, *141*, 4764–4774.

(30) Shu, C.; Pink, M.; Junghoefer, T.; Nadler, E.; Rajca, S.; Casu, M. B.; Rajca, A. Synthesis and Thin Films of Thermally Robust Quartet (S = 3/2) Ground State Triradical. *J. Am. Chem. Soc.* **2021**, *143*, 5508–5518. DOI: 10.1021/jacs.1c01305.

(31) Zhang, S.; Pink, M.; Junghoefer, T.; Zhao, W.; Hsu, S.-N.; Rajca, S.; Calzolari, A.; Boudouris, B. W.; Casu, M. B.; Rajca, A. High-Spin (S = 1) Blatter-Based Diradical with Robust Stability and Electrical Conductivity. *J. Am. Chem. Soc.* **2022**, *144*, 6059–6070. DOI: 10.1021/jacs.2c01141.

(32) Ovchinnikov, A. A. Multiplicity of the ground state of large alternant organic molecules with conjugated bonds. *Theor. Chim. Acta.* **1978**, *47*, 297–304.

(33) Gallagher, N. M.; Olankitwanit, A.; Rajca, A. High-Spin Organic Molecules. *J. Org. Chem.* **2015**, *80*, 1291–1298
(34) Nagata, A.; Hiraoka, S.; Suzuki, S.; Kozaki, M.; Shiomi, D.; Sato, K.; Takui, T.; Tanaka, R.; Okada, K. Redox-Induced Modulation of Exchange Interaction in a High-Spin Ground-State Diradical/Triradical System. *Chem. Eur. J.* **2020**, *26*, 3166–3172. DOI: 10.1002/chem.201905465
(35) Shiraishi, K.; Rajca, A.; Pink, M.; Rajca, S. π-Conjugated Conjoined Double Helicene via a Sequence of Three Oxidative CC- and NN-Homocouplings. *J. Am. Chem. Soc.* **2005**, *127*, 9312–9313.
(36) Rajca, A.; Miyasaka, M.; Pink, M.; Wang, H.; Rajca, S. Helically Annelated and Cross-Conjugated Oligothiophenes: Asymmetric Synthesis, Resolution, and Characterization of a Carbon-Sulfur [7]Helicene. *J. Am. Chem. Soc.* **2004**, *126*, 15211–1522, DOI: https://doi.org/10.1021/ja0462530
(37) Laleu, B.; Mobian, P.; Herse, C.; Laursen, B. W.; Hopfgartner, G.; Bernardinelli, G.; Lacour, J. Resolution of [4]Heterohelicenium Dyes with Unprecedented Pummerer-like Chemistry. *Angew. Chem. Int. Ed.* **2005**, *44*, 1879–1883. DOI: https://doi.org/10.1002/anie.200462321
(38) Rajca, A.; Miyasaka, M.; Pink, M.; Xiao, S.; Rajca, S.; Das, K.; Plessel, K. Functionalized Thiophene-Based [7]Helicene: Chirooptical Properties versus Electron Delocalization. *J. Org. Chem.* **2009**, *74*, 7504–7513. DOI: 10.1021/jo901769c
(39) Shen, C.; Anger, E.; Srebro, M.; Vanthuyne, N.; Deol, K. K.; Jefferson, T. D.; Muller, G.; Williams, J. A. G.; Toupet, L.; Roussel, C.; Autschbach, J.; Réau, R.; Crassous, J. Straightforward access to mono- and bis-cycloplatinated helicenes displaying circularly polarized phosphorescence by using crystallization resolution methods. *Chem. Sci.* **2014**, *5*, 1915–1927. DOI: https://doi.org/10.1039/C3SC53442A
(40) Vale, M.; Pink, M.; Rajca, S.; Rajca, A. Synthesis, Structure, and Conformation of Aza[1*n*]metacyclophanes. *J. Org. Chem.* **2008**, *73*, 27–35.
(41) Donohoe, T. J.; House, D. Ammonia Free Partial Reduction of Aromatic Compounds Using Lithium Di-*tert*-butylbiphenyl (LiDBB). *J. Org. Chem.* **2002**, *67*, 5015–5018.
(42) Donohoe, T. J.; Headley, C. E.; Cousins, R. P. C.; Cowley, A. Flexibility in the Partial Reduction of 2,5-Disubstituted Pyrroles: Application to the Synthesis of DMDP. *Org. Lett.* **2003**, *5*, 999–1002.
(43) Huang, S.; Paletta, J. T.; Elajaili, H.; Huber, K.; Pink, M.; Rajca, S.; Eaton, G. R.; Eaton, S. S.; Rajca, A. Synthesis and Electron Spin Relaxation of Tetracarboxylate Pyrroline Nitroxides. *J. Org. Chem.* **2017**, *82*, 1538–1544.
(44) Mourier, P. A.; Eliot, E.; Caude, M. H.; Rosset, R. H.; Tambute, A. G. Supercritical and Subcritical Fluid Chromatography on a Chiral Stationary Phase for the Resolution of Phosphine Oxide Enantiomers. *Anal. Chem.* **1985**, *57*, 2819–2823. DOI: https://doi.org/10.1021/ac00291a017
(45) Storch, J.; Kalíková, K.; Tesařová, E.; Maier, V.; Vacek, J. Development of separation methods for the chiral resolution of hexahelicenes. *J. Chromatography A* **2016**, *1476*, 130–134. DOI: https://doi.org/10.1016/j.chroma.2016.10.083
(46) Rajca, A.; Shiraishi, K.; Pink, M.; Rajca, S. Triplet (*S* = 1) Ground State Aminyl Diradical. *J. Am. Chem. Soc.* **2007**, *129*, 7232–7233.
(47) Boratynski, P. J.; Pink, M.; Rajca, S.; Rajca, A. Isolation of the Triplet Ground State Aminyl Diradical. *Angew. Chem., Int. Ed.* **2010**, *49*, 5459–5462.
(48) Rajca, A.; Olankitwanit, A.; Wang, Y.; Boratyński, P. J.; Pink, M.; Rajca, S. High-Spin *S* = 2 Ground State Aminyl Tetraradicals. *J. Am. Chem. Soc.* **2013**, *135*, 18205–18215.
(49) Zhang, H.; Pink, M.; Wang, Y.; Rajca, S.; Rajca, A. High-Spin *S* = 3/2 Ground-State Aminyl Triradicals: Toward High-Spin Oligo-Aza Nanographenes. *J. Am. Chem. Soc.* **2022**, *144*, 19576–19591.
(50) Stoll, S.; Schweiger, A. EasySpin, a comprehensive software package for spectral simulation and analysis in EPR. *J. Magn. Reson.* **2006**, *178*, 42–55. DOI: 10.1016/j.jmr.2005.08.013
(51) Rajca, A.; Olankitwanit, A.; Rajca, S. Triplet Ground State Derivative of Aza-*m*-Xylylene Diradical with Large Singlet–Triplet Energy Gap. *J. Am. Chem. Soc.* **2011**, *133*, 4750–4753. DOI: 10.1021/ja200708b
(52) Olankitwanit, A.; Pink, M.; Rajca, S.; Rajca, A. Synthesis of Aza-*m*-Xylylene Diradicals with Large Singlet-Triplet Energy Gap and Statistical Analyses of their EPR Spectra. *J. Am. Chem. Soc.* **2014**, *136*, 14277–14288. DOI: 10.1021/ja508119d
(53) Morton, J. R. Electron Spin Resonance Spectra of Oriented Radicals. *Chem. Rev*. **1964**, *64*, 453–471.
(54) Havlas, Z.; Michl, J. Ab initio calculation of zero-field splitting and spin-orbit coupling in ground and excited triplets of *m*-xylylene. *J. Chem. Soc., Perkin Trans. 2*, **1999**, 2299–2303. DOI: https://doi.org/10.1039/A906648I
(55) Havlas, Z.; Kývala, M.; Michl, J. Spin–orbit coupling in biradicals. 5. Zero-field splitting in triplet dimethylnitrenium, dimethylphosphenium and dimethylarsenium cations. *Mol. Phys.* **2005**, *103*, 407–411. DOI: https://doi.org/10.1080/00268970412331319245
(56) Sinnecker, S.; Neese, F. Spin–Spin Contributions to the Zero-Field Splitting Tensor in Organic Triplets, Carbenes and Biradicals - A Density Functional and Ab Initio Study. *J. Phys. Chem. A* **2006**, *110*, 12267–12275. DOI: 10.1021/jp0643303
(57) Neese, F. The ORCA program system. *Wiley Interdisciplinary Reviews: Comp. Mol. Sci.* **2012**, *2*, 73–78, DOI: 10.1002/wcms.81
(58) Frisch, M. J.; Trucks, G. W.; Schlegel, H. B.; Scuseria, G. E.; Robb, M. A.; Cheeseman, J. R.; Scalmani, G.; Barone, V.; Petersson, G. A.; Nakatsuji, H.; Li, X.; Caricato, M.; Marenich, A. V.; Bloino, J.; Janesko, B. G.; Gomperts, R.; Mennucci, B.; Hratchian, H. P.; Ortiz, J. V.; Izmaylov, A. F.; Sonnenberg, J. L.; Williams-Young, D.; Ding, F.; Lipparini, F.; Egidi, F.; Goings, J.; Peng, B.; Petrone, A.; Henderson, T.; Ranasinghe, D.; Zakrzewski, V. G.; Gao, J.; Rega, N.; Zheng, G.; Liang, W.; Hada, M.; Ehara, M.; Toyota, K.; Fukuda, R.; Hasegawa, J.; Ishida, M.; Nakajima, T.; Honda, Y.; Kitao, O.; Nakai, H.; Vreven, T.; Throssell, K.; Montgomery, J. A., Jr.; Peralta, J. E.; Ogliaro, F.; Bearpark, M. J.; Heyd, J. J.; Brothers, E. N.; Kudin, K. N.; Staroverov, V. N.; Keith, T. A.; Kobayashi, R.; Normand, J.; Raghavachari, R.; Rendell, A. P.; Burant, J. C.; Iyengar, S. S.; Tomasi, J.; Cossi, M.; Millam, J. M.; Klene, M.; Adamo, C.; Cammi, R.; Ochterski, J. W.; Martin, R. L.; Morokuma, K.; Farkas, O.; Foresman, J. B.; Fox, D. J. *Gaussian 16*, revision A.03; Gaussian, Inc.: Wallingford, CT, 2016.
(59) Rajca, S.; Rajca, A.; Wongsriratanakul, J.; Butler, P.; Choi, S. Organic Spin Clusters. Dendritic-Macrocyclic Polyarylmethyl Polyradical with Very High-Spin of *S* = 10 and its Derivatives: Synthesis, Magnetic Studies, and Small Angle Neutron Scattering. *J. Am. Chem. Soc.* **2004**, *126*, 6972–6986.
(60) Rajca, A. The Physical Organic Chemistry of Very High-Spin Polyradicals. *Adv. Phys. Org. Chem.* **2005**, *40*, 153–199.
(61) Groen, M. B.; Wynberg, H. Optical Properties of Some Heterohelicenes. Absolute Configuration. *J. Am. Chem. Soc.* **1971**, *93*, 2968–2974. DOI: 10.1021/ja00741a025
(62) Mori, T. Chiroptical Properties of Symmetric Double, Triple, and Multiple Helicenes. *Chem. Rev.* **2021**, *121*, 2373–2412.
(63) Miyasaka, M.; Pink, M.; Rajca, S.; Rajca, A. Noncovalent Interactions in the Asymmetric Synthesis of Rigid, Conjugated Helical Structures. *Angew. Chem. Int. Ed.* **2009**, *48*, 5954–5957. DOI: 10.1002/anie.200901349
(64) Dreher, S. D.; Katz, T. J.; Lam, K.-C.; Rheingold, A. L. Application of the Russig-Laatsch Reaction to Synthesize a Bis[5]helicene

Chiral Pocket for Asymmetric Catalysis. *J. Org. Chem.* **2000**, *65,* 815–822. DOI: 10.1021/jo991498u

(65) Zhang, S.; Liu, X.; Li, C.; Li, L.; Song, J.; Shi, J.; Morton, M.; Rajca, S.; Rajca, A.; Wang, H. Thiophene-Based Double Helices: Syntheses, X-ray Structures, and Chiroptical Properties. *J. Am. Chem. Soc.* **2016**, *138*, 10002–10010, DOI: 10.1021/jacs.6b05709

(66) Liu, Y.; Ma, Z.; Wang, Z.; Jiang, W. Boosting Circularly Polarized Luminescence Performance by a Double π-Helix and Heteroannulation. *J. Am. Chem. Soc.* **2022**, *144*, 11397−11404. DOI: https://doi.org/10.1021/jacs.2c04012

(67) Kiel, G. R.; Bergman, H. M.; Samkian, A. E.; Schuster, N. J.; Handford, R. C.; Rothenberger, A. J.; Gomez-Bombarelli, R.; Nuckolls, C.; Tilley, T. D. Expanded [23]-Helicene with Exceptional Chiroptical Properties via an Iterative Ring-Fusion Strategy. *J. Am. Chem. Soc.* **2022**, *144*, 51, 23421–23427. DOI: 10.1021/jacs.2c09555

(68) Uceda, R. G.; Cruz, C. M.; Míguez-Lago, S.; de Cienfuegos, L. A.; Longhi, G.; Pelta, D. A.; Novoa, P.; Mota, A. J.; Cuerva, J. M.; Miguel, D. Can Magnetic Dipole Transition Moment Be Engineered? *Angew. Chem. Int. Ed.* **2024**, *63*, e202316696. DOI: https://doi.org/10.1002/anie.202316696

(69) Ito, H.; Sakai, H.; Okayasu, Y.; Yuasa, J.; Mori, T.; Hasobe, T. Significant Enhancement of Absorption and Luminescence Dissymmetry Factors in the Far-Red Region: A Zinc(II) Homoleptic Helicate Formed by a Pair of Achiral Dipyrromethene Ligands. *Chem. Eur. J.* **2018**, *24*, 16889–16894. DOI: 10.1002/chem.201804171

(70) Martin, R. H.; Marchant, M. J. *Tetrahedron* **1974**, *30*, 347–349. DOI: 10.1016/S0040-4020(01)91469-3

(71) Goedicke, Ch.; Stegemeyer, H. Resolution and racemization of pentahelicene. *Tetrahedron Lett.* **1970**, *11*, 937–940. DOI: https://doi.org/10.1016/S0040-4039(01)97871-2

(72) Nakai, Y.; Mori, T.; Inoue, Y. Theoretical and Experimental Studies on Circular Dichroism of Carbo[n]helicenes. *J. Phys. Chem. A* **2012**, *116*, 7372–7385. DOI: https://doi.org/10.1021/jp304576g

(73) Chai, J. D.; Head-Gordon, M. Long-range corrected hybrid density functionals with damped atom-atom dispersion corrections. *Phys. Chem. Chem. Phys.* **2008**, *10*, 6615–6620.

(74) Yamaguchi, K.; Jensen, F.; Dorigo, A.; Houk, K. N. A Spin Correction Procedure for Unrestricted Hartree–Fock and Møller–Plesset Wavefunctions for Singlet Diradicals and Polyradicals. *Chem. Phys. Lett.* **1988**, *149*, 537–542.

(75) Trinquier, G.; Suaud, N.; Malrieu, J.-P. Theoretical Design of High-Spin Polycyclic Hydrocarbons. *Chem. Eur. J.* **2010**, *16*, 8762–8772.

(76) Quast, H.; Nüdling, W.; Klemm, G.; Kirschfeld, A.; Neuhaus, P.; Sander, W.; Hrovat, D. A.; Borden, W. T. A Perimidine-Derived Non-Kekulé Triplet Diradical. *J. Org. Chem.* **2008**, *73*, 4956–4961.

(77) Barone, V.; Cacelli, I.; Ferretti, A.; Prampolini, G. Quantitative prediction and interpretation of spin energy gaps in polyradicals: the virtual magnetic balance. *Phys. Chem. Chem. Phys.* **2017**, *19*, 9039–9044. DOI: 10.1039/C7CP00186J

(78) Barone, V.; Cacelli, I.; Ferretti, A. The role of the multiconfigurational character of nitronyl-nitroxide in the singlet–triplet energy gap of its diradicals. *Phys. Chem. Chem. Phys.* **2018**, *20*, 18547–18555. DOI: https://doi.org/10.1039/C8CP02165A

(79) Sugawara, T.; Komatsu, H.; Suzuki, K. Interplay between Magnetism and Conductivity Derived from Spin-Polarized Donor Radicals. *Chem. Soc. Rev.* **2011**, *40*, 3105–3118. DOI: 10.1039/c0cs00157k

(80) Gryn'ova, G.; Coote, M. L.; Corminboeuf, C. Theory and Practice of Uncommon Molecular Electronic Configurations. *WIREs Comput. Mol. Sci.* **2015**, *5*, 440–459. DOI: 10.1002/wcms.1233

(81) Murata, R.; Wang, Z.; Abe, M. Singly Occupied Molecular Orbital–Highest Occupied Molecular Orbital (SOMO–HOMO) Conversion. *Aust. J. Chem.* **2021**, *74*, 827–837. DOI: 10.1071/CH21186

(82) Kasemthaveechok, S.; Abella, L.; Crassous, J.; Autschbach, J.; Favereau, L. Organic Radicals with Inversion of SOMO and HOMO Energies and Potential Applications in Optoelectronics. *Chem. Sci.* **2022**, *13*, 9833–9847. DOI: 10.1039/D2SC02480B

(83) SAINT, Bruker Analytical X-Ray Systems, Madison, WI, current version.

(84) Blessing, R. An empirical correction for absorption anisotropy. *Acta Cryst. A* **1995**, *51*, 33–38.

(85) Altomare, A.; Cascarno, G.; Giacovazzo, C.; Gualardi, A. SIR-92. *J. Appl. Cryst.* **1993**, *26*, 343–350.

(86) SHELXTL-Plus, Bruker Analytical X-Ray Systems, Madison, WI, current version.

(87) Spek, A. L. PLATON *Acta Cryst. A* **1990**, *46*, C34.

(88) Rajca, A. Organic diradicals and polyradicals: from spin coupling to magnetism? *Chem. Rev.* **1994**, *94*, 871–893. DOI: 10.1021/cr00028a002

Insert Table of Contents artwork here

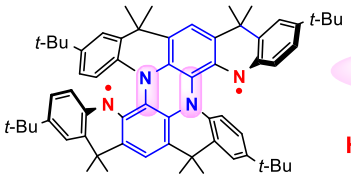

Chiral C_2-Symmetric

3-Electron C-N Bonds

Persistence at 293 K
High-Spin Ground State
ΔE_{ST} ~ 0.4 kcal mol^{-1}